

Supporting Information

Peudecerf et al. 10.1073/pnas.1702469114

SI Model

Equations for Surfactant-Laden Flows. We consider a 2D microchannel flow over a finite-length SHS, with the geometry presented in Fig. 2A. Because we maintained a flat plastron in the experiments, and the present focus is on Marangoni stresses, here we assume that the air–water interface is flat.

The continuity and Navier–Stokes equations for the flow of mass and momentum are coupled with the transport equation for a surfactant. The 2D velocity field is $\mathbf{u} = (u, w)$ for the (x, z) directions, and the surfactant concentration field is c . The fluid has density ρ , as well as dynamic and kinematic viscosities μ and ν , respectively. The surfactant has bulk diffusivity D . The transport equations are, in dimensional form,

$$\nabla \cdot \mathbf{u} = 0, \quad [\text{S1}]$$

$$\frac{\partial \mathbf{u}}{\partial t} + \nabla \cdot (\mathbf{u}\mathbf{u}) = -\frac{\nabla p}{\rho} + \nu \nabla^2 \mathbf{u}, \quad [\text{S2}]$$

$$\frac{\partial c}{\partial t} + \nabla \cdot (\mathbf{u}c) = D \nabla^2 c. \quad [\text{S3}]$$

The inlet and outlet conditions at $x = 0$ and $x = g + \ell$ respectively consist of a Poiseuille flow with mean velocity U and maximum velocity u_{\max} , such that

$$u(z) = 6U \frac{z}{H} \left(1 - \frac{z}{H}\right), \quad [\text{S4}]$$

whereas the inlet has a specified bulk concentration $c = c_0$, and at the outlet we set

$$\frac{\partial c}{\partial x} = 0. \quad [\text{S5}]$$

On the solid surfaces at $z = 0$ (top boundary or SHS side in Fig. 2A) and $z = -H$ (bottom boundary)

$$\mathbf{u} = \mathbf{0}, \quad [\text{S6}]$$

$$\frac{\partial c}{\partial z} = 0. \quad [\text{S7}]$$

At the plastron, an adsorption/desorption model is used to couple the surfactant transport between the bulk and the interface

$$D \frac{\partial c}{\partial z} \Big|_I = -S(c_I, \Gamma), \quad [\text{S8}]$$

$$\frac{\partial \Gamma}{\partial t} + \frac{\partial(u_I \Gamma)}{\partial x} = D_s \frac{\partial^2 \Gamma}{\partial x^2} + S(c_I, \Gamma), \quad [\text{S9}]$$

where Γ is the interfacial concentration, D_s is the surface diffusivity, the subscript I denotes quantities at the interface, and $S(c_I, \Gamma)$ encapsulates the adsorption model. In practice, the choice of adsorption kinetics is of relatively weak importance, because surfactant effects are already very strong at extremely low surfactant concentrations (shown in Fig. 2 and Fig. S1). For such low values of concentration, different kinetics models are essentially equivalent (40). For definiteness, here we use Frumkin kinetics

$$S(c_I, \Gamma) = \kappa_a c_I (\Gamma_m - \Gamma) - \kappa_d \Gamma e^{A\Gamma/\Gamma_m}, \quad [\text{S10}]$$

where κ_a, κ_d are the adsorption and desorption coefficients, Γ_m is the maximum packing interfacial concentration, and A is the interaction coefficient (39). On the air–water interface, the velocity field is coupled to the interfacial surfactant distribution through a balance between viscous and Marangoni stresses (45)

$$w = 0, \quad [\text{S11}]$$

$$\mu \frac{\partial u}{\partial z} \Big|_I = -nRT \left(\frac{\Gamma_m}{\Gamma_m - \Gamma} + A \frac{\Gamma}{\Gamma_m} \right) \frac{\partial \Gamma}{\partial x}, \quad [\text{S12}]$$

where n is the surfactant style constant (40), R is the universal gas constant, and T is the absolute temperature. The boundary condition for Γ , where the interface meets each solid boundary at a stagnation point on the top boundary $z = 0$ (i.e., upstream stagnation point, $x = \ell/2$, and downstream stagnation point, $x = g + \ell/2$; Fig. 2A), is given by

$$\frac{\partial \Gamma}{\partial x} = 0. \quad [\text{S13}]$$

We can nondimensionalize Eqs. S1–S3, S9, and S10 and the boundary conditions S4–S8 and S11–S13 to reveal nine characteristic nondimensional numbers for this problem. Using g as a characteristic length scale, U as a characteristic velocity scale, g/U as a characteristic time scale, ρU^2 as a characteristic pressure scale, c_0 as a characteristic bulk concentration scale, and Γ_m as a characteristic interfacial concentration scale, we obtain the nondimensional conservation equations for mass, momentum, bulk surfactant, and interfacial surfactant (where hats denote nondimensional quantities),

$$\nabla \cdot \hat{\mathbf{u}} = 0, \quad [\text{S14}]$$

$$\frac{\partial \hat{\mathbf{u}}}{\partial \hat{t}} + \nabla \cdot (\hat{\mathbf{u}}\hat{\mathbf{u}}) = -\nabla \hat{p} + \frac{\hat{H}}{Re} \nabla^2 \hat{\mathbf{u}}, \quad [\text{S15}]$$

$$\frac{\partial \hat{c}}{\partial \hat{t}} + \nabla \cdot (\hat{\mathbf{u}}\hat{c}) = \frac{1}{Pe} \nabla^2 \hat{c}, \quad [\text{S16}]$$

$$\frac{\partial \hat{\Gamma}}{\partial \hat{t}} + \frac{\partial(\hat{u}_I \hat{\Gamma})}{\partial \hat{x}} = \frac{1}{Pe_s} \frac{\partial^2 \hat{\Gamma}}{\partial \hat{x}^2} + \hat{S}(\hat{c}_I, \hat{\Gamma}), \quad [\text{S17}]$$

where the source–sink concentration flux at the interface is

$$\hat{S}(\hat{c}_I, \hat{\Gamma}) = Bi \left[k \hat{c}_I (1 - \hat{\Gamma}) - e^{A\hat{\Gamma}} \hat{\Gamma} \right]. \quad [\text{S18}]$$

At the inlet $\hat{x} = 0$, the boundary conditions are, in nondimensional form,

$$\hat{u} = \frac{6\hat{z}}{\hat{H}} \left(1 - \frac{\hat{z}}{\hat{H}}\right), \quad [\text{S19}]$$

$$\hat{w} = 0, \quad [\text{S20}]$$

$$\hat{c} = 1. \quad [\text{S21}]$$

At the outlet $\hat{x} = 1 + \hat{\ell}$,

$$\hat{u} = \frac{6\hat{z}}{\hat{H}} \left(1 - \frac{\hat{z}}{\hat{H}}\right), \quad [\text{S22}]$$

$$\hat{w} = 0, \quad [\text{S23}]$$

$$\frac{\partial \hat{c}}{\partial \hat{x}} = 0. \quad [\text{S24}]$$

On the solid surfaces at $\hat{z} = 0$ and $\hat{z} = -\hat{H}$,

$$\hat{\mathbf{u}} = \mathbf{0}, \quad [\text{S25}]$$

$$\frac{\partial \hat{c}}{\partial \hat{z}} = 0. \quad [\text{S26}]$$

On the air–water interface at $\hat{z} = 0, \hat{\ell}/2 \leq \hat{x} \leq \hat{\ell}/2 + 1$,

$$\hat{w} = 0, \quad [\text{S27}]$$

$$\frac{\chi k}{Pe} \frac{\partial \hat{c}}{\partial \hat{z}} \Big|_I = -\hat{S}(\hat{c}_I, \hat{\Gamma}), \quad [\text{S28}]$$

$$\frac{\partial \hat{u}}{\partial \hat{z}} \Big|_I = -Ma \left(\frac{1}{1 - \hat{\Gamma}} + A\hat{\Gamma} \right) \frac{\partial \hat{\Gamma}}{\partial \hat{x}}, \quad [\text{S29}]$$

$$\frac{\partial \hat{\Gamma}}{\partial \hat{x}} = 0 \quad \text{at } \hat{x} = \hat{\ell}/2, 1 + \hat{\ell}/2. \quad [\text{S30}]$$

The Reynolds number is $Re = HU/\nu$, based on the transverse length scale H instead of the longitudinal length scale g . For the internal channel flow considered in this study, H is the appropriate length scale to determine the flow regime, which is Stokes flow ($Re \lesssim 1$) for all our experiments and numerical simulations. The bulk and surface Péclet numbers are $Pe = gU/D$ and $Pe_s = gU/D_s$. The nondimensional bulk concentration is $k = \kappa_a c_0 / \kappa_d$. The Biot number is $Bi = \kappa_d g / U$. The kinetics are parameterized by $\chi = \kappa_d / (\kappa_a \Gamma_m)$. The Marangoni number is $Ma = nRT\Gamma_m / (\mu U)$. We note that there are also two geometrical nondimensional numbers: the aspect ratio of the channel $\hat{H} = H/g$ and the proportion of solid surface to free surface on the SHS side $\hat{\ell} = \ell/g$. With nine nondimensional parameters, of which six depend on the physical and kinetic properties of the surfactant, the full transport problem related to surfactant-contaminated SHSs is effectively very complex.

The nondimensional numbers of all our experiments and simulations are presented in Tables S2, S4, and S7. We have also computed two other useful nondimensional ratios (41): $D = \chi(1 + k)/Pe^{1/2}$, the ratio of the diffusive flux of surfactants across the diffusive boundary layer to the convective flux along the air-water interface (which is based on [S16] at steady state), and $\mathcal{K} = Bi(1 + k)$, the ratio of the adsorption/desorption kinetics flux to the convective flux along the interface (which is based on [S18]). A discussion of the scaling analysis of the equations above and their characteristic nondimensional numbers is provided in *SI Analysis and Discussion of Characteristic Nondimensional Numbers*.

SI Materials and Methods

Two-Dimensional Surfactant-Laden Simulations. The model presented above was implemented in COMSOL Multiphysics in a 2D finite-element numerical simulation. The geometry corresponding to Fig. 2A was created using the values for the gap length g , the ridge length ℓ , the chamber height H , and the maximum forcing speed of the Poiseuille flow u_{\max} presented in Table S1. All other relevant physical and kinetic parameters of the simulations are presented in Table S1 and correspond to the well-characterized surfactant SDS. Note that in *Supporting Information*, we use interchangeably $\text{mol}\cdot\text{m}^{-3}$ and mM as equal units for surfactant bulk concentrations. The SDS properties are well described by Frumkin kinetics (39). Nondimensional numbers associated with these 2D simulations are listed in Table S2.

When designing the mesh of the domain, we were particularly careful about strong possible variations of some variables near the stagnation points at the beginning and end of the gap. The maximum size of elements near these points is equal to $0.01 \mu\text{m}$. For all simulations with $g < 1 \text{ mm}$, the maximum element size on the interface is $0.05 \mu\text{m}$. For simulations with $g = 1 \text{ mm}$ and 2 mm , the maximum element size on the interface is $0.2 \mu\text{m}$. Finally, for $g = 5 \text{ mm}$ and 10 mm , a coarser mesh is used in the central part of the interface, 1 mm away from the endpoints, with a maximum element size of $2 \mu\text{m}$. In the bulk, the maximum element size is $10 \mu\text{m}$ for all simulations.

To implement the model, we combine the laminar flow module with a dilute species transport module of COMSOL for the transport equations in the bulk (Eqs. S1–S3). The equation for the transport of surfactant on the interface (Eq. S9) is imple-

mented through a general form boundary partial differential equation, with a source term corresponding to the kinetics flux S . This flux also serves to implement the boundary condition S8 at the interface for the dilute species transport module. The Marangoni forces resulting from the nonuniform distribution of surfactants at the interface modify the laminar flow, as stated in [S12], through a weak contribution at the interface coupled to a free-slip boundary condition.

The flow in the simulated chamber is forced by an inlet velocity boundary condition corresponding to a Poiseuille velocity profile $u(z) = 4u_{\max}z(H-z)/H^2$ (with $u_{\max} = 3U/2$). The initial guess velocity profile for the stationary solver is set to this reference Poiseuille profile in the entire chamber.

To increase the accuracy of the computation, we discretize the fluid flow with quadratic elements for the velocity field and linear elements for the pressure field and quadratic elements for the concentration field in the bulk and the concentration field on the interface.

We use the MUMPS solver of COMSOL to solve for the steady state of the system, with a relative tolerance of 10^{-5} .

To check how the results obtained would change for surfactants of different strengths, we also ran simulations for two extreme sets of parameters values for the surfactant choice, using the Frumkin kinetics framework (Fig. S1). The first set corresponds to a model of strong surfactant with high affinity to the interface and low diffusivity ($\kappa_d = 1 \text{ s}^{-1}$, $\kappa_a = 10^6 \text{ m}^3 \cdot \text{mol}^{-1} \cdot \text{s}^{-1}$, $\Gamma_m = 10^{-5} \text{ mol}\cdot\text{m}^{-2}$, $A = -3$, $D = D_s = 10^{-11} \text{ m}^2 \cdot \text{s}^{-1}$), the second set corresponds to a model of weak surfactant with weak affinity to the interface and high diffusivity that promotes the smoothing of any interfacial gradients ($\kappa_d = 100 \text{ s}^{-1}$, $\kappa_a = 10^{-1} \text{ m}^3 \cdot \text{mol}^{-1} \cdot \text{s}^{-1}$, $\Gamma_m = 10^{-6} \text{ mol}\cdot\text{m}^{-2}$, $A = 3$, $D = D_s = 10^{-9} \text{ m}^2 \cdot \text{s}^{-1}$). These parameters were typically selected from the extreme values of the data reported in tables 1 and 3 in ref. 40. We performed simulations with the rest of the parameters as in the simulation for Fig. 2D, except for the bulk concentration c_0 whose range was extended to cover the transitions for the strong and weak surfactants, respectively (see Tables S1 and S2 for all of the parameter values and associated nondimensional numbers, respectively). For both cases, we observe progressive immobilization of the interface and increase of viscous stress with increasing bulk concentration of surfactant (Fig. S1). For the strong surfactant (plotted with blue symbols), the transition toward a no-slip boundary condition occurs at minute concentrations, below $c_0 \approx 10^{-12} \text{ mM}$ and well below the transition value for SDS ($c_0 \approx 10^{-4} \text{ mM}$). For the weak surfactant (plotted with green symbols), the transition occurs at $c_0 \approx 1 \text{ mM}$, which is much higher than for SDS. In general, one cannot of course guarantee that no traces of strong surfactants are present in a given flow.

Three-Dimensional Surfactant-Free Simulations. To obtain a reference flow profile for long rectangular gratings located on one side of a 3D microchannel, in the idealized case of pure water ($c_0 = 0$), we solved the Navier–Stokes equations using COMSOL Multiphysics. The aim is to compare these clean-case or surfactant-free simulations with the two steady-state forcing experiments shown in Fig. 3D and E with symbols (numerical results are shown with solid lines). Our 3D numerical domain corresponds to the portion of a microchannel below half of a grating element, with plane of symmetry ($x, y = w/2, z$) (Fig. 2B and C). We use symmetry boundary conditions on each side of the domain to solve for the flow on a large number of parallel gratings as in the experiment. All of the parameters for these two simulations, with $g = 2 \text{ mm}$ and 30 mm in Fig. 3D and E, respectively, are detailed in Table S5. The numerical parameters are chosen to match the experimental conditions, assuming a surfactant-free flow. No-slip boundary conditions are imposed on the ridges, whereas free slip is imposed on the plastron. The flow

was forced by a 2D Poiseuille profile $u(z) = 4u_{\max}z(H - z)/H^2$ with $u_{\max} = 120 \mu\text{m}\cdot\text{s}^{-1}$. All of the experiments being conducted at low Reynolds number in the Stokes regime, we note that the normalized velocity profiles presented in Fig. 3 *D* and *E* do not depend on u_{\max} or U . This same velocity profile was also chosen as an initial guess for the steady-state solution. Water viscosity was $\mu = 9.3 \times 10^{-4} \text{ N}\cdot\text{s}\cdot\text{m}^{-2}$, corresponding to the water temperature of 23 °C measured in the laboratory during the steady-state forcing experiments. We use a Physics-controlled mesh with finer to extrafine element size, with a linear discretization of elements and further local refinement of meshing around the areas of interest if required.

SI Experimental Protocols

Cleaning Protocols. Two different cleaning protocols were followed in the preparation of the experiments. For both cleaning protocols, as well as all of the experiments conducted, only purified water (using the Milli Q water purification system; EMD Millipore) at 23 °C with resistivity 18.2 M Ω -cm and less than 5 parts per billion of total organic content was used.

A strict 10-d cleaning protocol was designed in an attempt to avoid any contamination of the microchannel, which could induce surfactant Marangoni stresses. The cleaning and experimental preparation were performed using laboratory coats and thoroughly washed nitrile gloves (Fisherbrand) (we note that standard laboratory gloves have traces of chemicals on their surface, which induce surfactant Marangoni stresses). The preparation of the PDMS (Sylgard 184) microchannels was done in a clean room. In this protocol, apart from the PDMS, only materials that could be cleaned thoroughly were used for the surfaces that were in contact with water during the experiments. In particular, all common plastic materials were avoided as they tend to release chemical traces with a surfactant effect when in contact with water. All tubings were made of fluorinated ethylene propylene (FEP) (0.5 mm internal diameter; The Dolomite Center Ltd.), connectors were made of stainless steel, the syringes (Gastight Hamilton) used to handle water and the microbead suspension were made of glass and polytetrafluoroethylene and fitted with stainless steel needles (24-gauge injection needles; Carl Roth GmbH), and the inlet and outlet reservoirs were made of glass. All of the tubings, connectors, needles, and reservoirs underwent five washing, rinsing, and curing cycles over a 10-d period before the experiments. The curing containers were large glass beakers that had been cleaned in an acid rinse dishwasher and further rinsed for 5 min with purified water. During the curing process, all of the beakers were covered to reduce contamination from the air. On the day of the experiments, all of the tubings and reservoirs were washed again with purified water. Washed metal tweezers were used to handle tubings and connectors to avoid touching surfaces that could be in contact with the water flowing through the microchannel. The fluorescent microbeads (LifeTechnologies FluoSphere carboxylate 0.5- μm diameter yellow/green 505/515) used to perform μ -PIV were washed and rinsed 10 times with purified water to dilute significantly any potential surfactant contamination traces. The coverslip forming the base of the microchannel was washed with abundant purified water and then air dried.

This strict cleaning protocol was followed only when conducting some steady-forcing experiments. The results, similar to those presented in Fig. 3*D* (conducted following the normal cleaning protocol described below), showed no or little slip in comparison with theoretical and numerical predictions with surfactant-free flows. As we show in Fig. 2*D*, the level of contamination necessary to induce surfactant Marangoni stresses is extremely small, of the order of 10^{-4} mM for the SDS surfactant. Moreover, as we show in Fig. S1, SDS is not the strongest surfactant and can be considered as inducing mild Marangoni stresses (see tables 1 and 3 in ref. 40, for a comparison of a broad range

of surfactants). Therefore, it is very likely that, even following this strict cleaning protocol, sufficient traces of chemicals with a surfactant effect contaminated our experiments. We believe that the most likely source of contamination in our experiments is the PDMS and its associated impurities. Un-cross-linked PDMS chains or impurities trapped in the PDMS could have a surfactant effect as has been observed in ref. 46. Contamination could also come from other sources, which might simply be unavoidable in normal laboratory conditions.

As surfactant contaminations were simply unavoidable in our experiments, a less time-consuming cleaning protocol was used for all of the experimental results presented in this study. We used flexible tubing (Tygon ND-100-80) instead of the FEP tubing, which was more difficult to handle due to its rigidity. The outlet and inlet reservoirs were replaced by polypropylene tubes (Eppendorf) or plastic syringes (BD Plastipack). All of the other elements of the apparatus, preparation tools, and materials were the same. Furthermore, cleaning of the tools, materials, tubings, connectors, and reservoirs was performed on the day of the experiment. They were all washed with plenty of purified water: typically with at least 10 times the volume they can contain. The fluorescent microbeads were washed at least 3 times.

Steady-Forcing Experiments. For steady-forcing experiments, the chamber was first filled with the suspension of microbeads, taking great care to avoid trapping any air bubble in the tubing or in the chamber. To obtain a low level of flow rate in the chamber while allowing accurate positioning of the inlet reservoir with respect to the outlet reservoir, a constriction was introduced on the hydraulic line by mounting a 30-gauge polypropylene syringe tip (Adhesive Dispensing Ltd.) on the inlet reservoir (syringe from BD Plastipack). Using a manual linear stage, the inlet reservoir was moved vertically after initial filling of the chamber until no flow could be observed in the middle of the chamber. This corresponded to the level of zero pressure gradient along the microfluidic line. The inlet position was then shifted by $5 \text{ mm} \pm 10 \mu\text{m}$, using the linear manual stage. Imaging was then performed in the central longitudinal portion of the gratings. Stacks of 30 successive images were taken at ≈ 10 fps at different z positions in the chamber and at different time points for each experiment. Once a microchannel was successfully prepared to conduct a series of experiments, most of the plastrons of the SHS gratings remained stable for ≈ 2 h.

The details of the parameters for the experiments presented in Fig. 3 *D* and *E* are described in Table S3. All of the nondimensional numbers associated with these experiments are presented in Table S4. As the type of surfactant that contaminated these experiments is unknown, we have assumed the same properties as the weak and strong surfactants whose physical and kinetics properties are described in Table S1. We have also assumed a broad concentration range for both surfactants, from $10^{-12} \text{ mol}\cdot\text{m}^{-3}$ to $1 \text{ mol}\cdot\text{m}^{-3}$. This gives us a broad range of values for the different nondimensional numbers. The mean forcing speed U was calculated from the experimental velocity profile by fitting a parabolic profile $u(z) = 6Uz(H - z)/H^2$ to the data.

Pressure-Relaxation Experiments. The protocol for each experiment had two phases: an initial loading phase with strong background flow and then a second phase without background flow to measure the surfactant Marangoni-driven backflow. During the initial loading phase the flow was driven at a very high background pressure gradient, to transport any surfactant along the air-water interface to the downstream stagnation end of a grating. This phase lasts for 4 min, during which images of the flow field were taken at different heights in the channel to obtain the vertical distribution of the stream-wise velocity profile. A typical velocity profile measured during the loading phase of the experiment shown in Fig. 4*A* is presented in Fig. S2. As the exposure

time on the camera was smaller but of the same order of magnitude as the typical time for the fluorescent particles to cross the field of view, particles were seen as streaks of dots on each image. The dots forming the streaks originate from the imaging by the spinning disk used with the microscope. The velocity profile was obtained by measuring the mean length of the fluorescent particle streaks on the image and dividing by the exposure time. As we can see in Fig. S2, the velocity profile measured in a vertical plane centered in the middle of a grating does not show any significant slip velocity at the air–water interface. We note that the spatial resolution and the technique to measure the velocity were not designed to measure accurately the velocity close to the plastron, as was done in the steady-forcing experiments (previous section and Fig. 3). The aim here was to obtain an estimate of the mean flow field in the microchannel. The profile follows a classical 2D Poiseuille profile, from which we computed the mean load speed U plotted in Fig. 4C.

In the second phase, the background pressure gradient was suppressed to stop the flow. Images of the flow field were recorded at a distance of $z = -4 \mu\text{m} \pm 1 \mu\text{m}$ from the air–water interface. Images were recorded for 1 min or 2 min starting ≈ 5 s before the background pressure gradient was suppressed (this corresponds to $t = 0$ in Fig. 4A, B, and D), at a frame rate of around 24 frames per second. See the snapshot corresponding to Movie S1 as an example. These images were then analyzed with μ -PIV, as explained in *Materials and Methods*, to produce the velocity fields, such as the one displayed in Fig. 4A. Then, the experiment was repeated but with imposing a negative background pressure gradient in the microchannel to produce an opposite flow. We could thus verify that the effect observed was independent of the flow direction in the initial loading phase.

The apparatus and the microchannels were prepared following the initial steps of the protocol described in the previous section. Then, to control the background pressure gradient imposed in the microchannel during the loading phase and ensure a rapid and smooth transition between the two phases, the inlet reservoir was attached at midheight onto a 150-mm motorized stage (Thorlabs NRT150/M) driven by a precision controller (Thorlabs APT BSC201, with $2 \mu\text{m}$ precision; maximum acceleration, $50 \text{ mm}\cdot\text{s}^{-2}$; maximum speed, $50 \text{ mm}\cdot\text{s}^{-1}$). This midheight constituted our zero elevation reference. The outlet reservoir was attached onto the fixed part of the motorized stage, which was itself attached onto a millimetric precision vertical ramp. Adjusting the height of the motorized stage effectively controlled the hydrostatic pressure in the microchannel and thus the interfacial deflection of the plastron. An initial upward loading phase was conducted, without recording any images, to determine accurately the level of zero background pressure gradient required for the second phase. Indeed, during this first loading phase where the inlet reservoir was raised to a given height ($\Delta H_r > 0$) compared with the outlet reservoir, water transferred from the inlet reservoir to the outlet reservoir. This led to a slight increase in the neutral elevation of the inlet reservoir corresponding to a zero background pressure required for the second phase. Then, to avoid complete depletion of the inlet reservoir by having flow in one direction only for all of the experiments, the next loading phase was conducted with a flow in the opposite direction, by lowering the inlet reservoir to a negative or opposite elevation ($\Delta H_r < 0$) of the exact same distance as in the upward loading phase. At the end of this first downward loading phase, which also lasts exactly 4 min, the inlet reservoir could simply be returned to the original zero reference elevation, having transferred back to the inlet reservoir the same amount of water that was depleted during the upward loading phase. The neutral elevations at the end of the upward and downward loading phases were found with an accuracy of 2–3 μm , which produced a very small flow below the level of detection of the μ -PIV system. This cycle was then repeated four times, with

images recorded during the loading phase to measure the velocity of the backflow.

The experimental parameters of all of the pressure-relaxation experiments are presented in Table S6. All of the nondimensional numbers associated with these experiments are presented in Table S7. Similar to the steady experiments, as the type of surfactant that contaminated these experiments is unknown, we have assumed the same properties as the weak and strong surfactants whose kinetics properties are described in Table S1. We have also assumed a broad concentration range for both surfactants, from $10^{-12} \text{ mol}\cdot\text{m}^{-3}$ to $1 \text{ mol}\cdot\text{m}^{-3}$. This gives us a broad range of values for the different nondimensional numbers. Note that by convention the background flow mean speed U is always considered positive, independently of the flow direction in the microchannel, so that the backflow is always negative, as shown in Fig. 4A and B. To indicate whether the loading phase was conducted upward or downward, ΔH_r is shown as positive or negative, respectively. As can be noted, there is a small asymmetry of $\sim \pm 5\%$ between the mean flow speeds of an upward loading phase and a downward loading phase. This is due to a different spatial arrangement of the tubings between the two loading phases. We also note that not all experiments could be exploited quantitatively. Due to the strong pressure change at the end of the loading phase, the plastron of some gratings failed and led to their wetting. Wetting could affect either the grating under study or an adjacent grating (notes in Table S6). With adjacent grating failure, the backflow was still observed on the remaining plastron, with qualitatively similar magnitude and time scale, but the backflow velocity was affected through viscous stresses in the water. These data were therefore not quantitatively accurate and have not been included in the graphs presented in Fig. 4C and D. The contrast between the flow field of a nonwetted grating and that of a wetted grating is also very clear when stopping the background pressure gradient. Similar to the flow above a ridge, the flow in the wetted grating stops immediately at the end of the loading phase, showing no backflow (Movie S2, which corresponds to Experiments 2–4 in Table S6).

Impact of Thermal Marangoni Effects in Experiments. We assess the potential impact of thermal Marangoni effects in our experiments to examine whether the backflow observed in the pressure-relaxation experiments could be due to thermal Marangoni effects. We distinguish steady temperature gradients from flow-dependent gradients.

Steady temperature gradients can arise due to spatial temperature variations in the setup close to the microchannel. As the backflow was observed in both flow directions through the microchannel, within a few minutes' interval, this implies that a steady spatial temperature gradient did not affect the experiments.

Temperature gradients could also arise due to heat being advected by the flow during the loading phase. This heat could come from the laser, although we note that its power was already very small, less than $155 \mu\text{W}$, and only a small fraction would have been absorbed as heat by water. As the microchannel height is only $H \approx 0.1 \text{ mm}$, the time scale for thermal diffusion across H is of the order of $H^2/D_T \approx 0.1 \text{ s}$, where $D_T \approx 1.4 \times 10^{-7} \text{ m}^2\cdot\text{s}^{-1}$ is the thermal diffusivity of water. Because the bottom of the microchannel is maintained at a fixed temperature by a Peltier element, as soon as the loading phase ends the temperature variations in the microchannel should vanish within $\sim 0.1 \text{ s}$. However, the time scales for the backflow are typically of the order of 1 min. Therefore, thermal Marangoni effects had negligible impact in our experiments.

SI Analysis and Discussion of Characteristic Nondimensional Numbers

The problem of surfactant-contaminated SHSs is a complex transport problem involving several coupled nonlinear partial

differential equations (Eqs. S14–S17). In addition, at the air–water interface a flux continuity condition S28 couples the bulk concentration and the interfacial concentration, and a stress continuity condition S29 couples the viscous force and the interfacial concentration gradient (i.e., Marangoni effect). To understand the effects of geometry, surfactant concentration or changes in surfactant properties on the drag reduction performance of the SHS through the scaling analysis of these equations is therefore a nontrivial exercise. Nevertheless, a few remarks can be made to explain, at least qualitatively, the main results of our study. The key results are that (i) only very small amounts of surfactants are needed to drastically reduce the drag reduction performance of SHSs (shown numerically and suggested by our careful experimental trial) and (ii) free slip at the air–water interface can be recovered when increasing the length of the gap g (shown numerically and experimentally).

From [S29], the air–water interface becomes a no-slip boundary if the velocity gradient at the interface scales as $\partial \hat{u} / \partial \hat{z} \sim 1 / \hat{H}$ (with $\hat{H} = H/g$). Assuming that the interfacial concentration gradient scales as $\partial \hat{\Gamma} / \partial \hat{x} \sim \langle \hat{\Gamma} \rangle$ (with $\langle \hat{\Gamma} \rangle$ the average concentration over the gap), we find that

$$\langle \hat{\Gamma} \rangle \sim \frac{g}{HMa}. \quad [\text{S31}]$$

Even when assuming extremely weak surfactant properties, the Marangoni number is very large in all our experiments and numerical simulations, $Ma \sim 10^3$ – 10^6 . We note that Ma is based on the maximum packing concentration Γ_m instead of a measure of the actual interfacial concentration, which is unknown. Hence, Ma represents the maximum possible value in the limit $\hat{\Gamma} \rightarrow 1$. Large Ma values imply that no slip at the interface can be achieved for $\langle \hat{\Gamma} \rangle \ll 1$. Although the relationship between the c_0 and Γ is rather complex through the diffusive boundary layer, the kinetics flux, and various couplings, this suggests that the threshold for the bulk surfactant contaminant c_0 is also very small. This is in agreement with our key finding *i*. Also, [S29] and [S31] show that increasing the gap length g , while maintaining all other parameters constant, will eventually lead to an increase in slip at the SHS. This is in agreement with our key finding *ii*.

Eqs. S29 and S31 suggest a linear relationship between the slip velocity at the interface and the interfacial concentration, at least for low $\langle \hat{\Gamma} \rangle$. However, we have found in Fig. 2D and [S1] that the transition from no slip to free slip at the SHS is strongly nonlinear, regardless of the type of surfactant. Similarly, the transition due to changes in gap length shown in Fig. 2E is also nonlinear. This is characteristic of the strong nonlinear couplings between the velocity field, the bulk concentration, and the interfacial concentration in this problem. It also shows the limits of our scaling analysis, where we assumed a simple linear profile for Γ . The authors of ref. 41 describe the different regimes for the surfactant concentration distribution at the interface of air bubbles rising in surfactant-contaminated water. Their axisymmetric problem is similar to our 2D problem, considering the top and bottom of the bubble as the upstream and downstream stagnation points of our SHS. The regimes they describe, based on the surfactant-related nondimensional parameters, relate the interfacial surfactant distribution with the flow at the macroscopic scale. If $\mathcal{D} \sim 1$ and $\mathcal{K} \sim 1$ [where $\mathcal{D} = \chi(1+k)/Pe^{1/2}$ is the ratio of the diffusive flux of surfactants across the diffusive boundary layer to the convective flux along the interface, and $\mathcal{K} = Bi(1+k)$ is the ratio of the adsorption/desorption kinetics flux to the convective flux along the interface], then the interfacial concentration gradient is approximately uniform (i.e., the concentration profile is linear) along most of the interface. This is known as the “uniformly retarded regime.” If $\mathcal{D} \ll 1$ or $\mathcal{K} \ll 1$ and $Pe_s \gg 1$, the interface is in the stagnant cap regime, characterized by a depletion of sur-

factant in the upstream part of the interface, a sharp nonlinear increase of the interfacial concentration, and an accumulation of surfactant near the downstream stagnation point.

According to the results displayed in Table S2, all our numerical simulations (Fig. 2 and Fig. S1) are in a transition regime between the uniformly retarded regime and the stagnant cap regime, except for the strong model surfactant (Fig. S1) that is in the stagnant cap regime. This means that the surfactant distribution is neither constant nor linear along the interface. Marangoni stresses can therefore develop due to concentration gradients along the interface in all our experiments.

Although the type of surfactants and their concentration are unknown in all our experiments (Figs. 3 and 4), we have estimated ranges for all of the nondimensional numbers in Tables S4 and S7, using the physical and kinetics properties of the weak and strong model surfactants described in Table S1 and assuming a broad range of concentration from $c_0 = 10^{-12}$ to $1 \text{ mol}\cdot\text{m}^{-3}$. The dimensional numbers show that all our experiments are most likely in a transition regime, similar to the results found for our numerical simulations. Only if the contaminant present in our experiments had the same properties as the strong model surfactant and its concentration was less than $\approx 0.1 \text{ mol}\cdot\text{m}^{-3}$ would the experiments be in the stagnant cap regime. Thus, the numerical simulations with SDS as contaminant appear to be an appropriate model for this problem.

Therefore, the analysis of the nondimensional characteristic numbers confirms the main conclusions of our study. Surfactant contaminants at very small concentrations can induce Marangoni stresses at the air–water interface of the SHS through a nonuniform concentration distribution established by the flow. The surfactant distribution is most likely in a nonlinear transition regime between the uniformly retarded regime and the stagnant cap regime. Marangoni stresses at the SHS can be reduced if the distance between the two stagnation points is larger than a critical value, which appears to be a nonlinear function of the interfacial concentration distribution, the Marangoni number, and the channel height.

SI Model for Pressure-Relaxation Experiments

We develop a model that predicts the temporal scale for the rapid backflow that we observed in the pressure-relaxation experiments (Fig. 4). We consider the geometry described in Fig. 2A, with the flow in the loading phase in the positive direction. We assume that the backflow observed at the end of the loading phase and developing in the negative direction is dominated by advection and thus neglect diffusion along the interface and the adsorption–diffusion flux between the interface and the bulk. These assumptions correspond to the stagnant cap regime where $Pe_s \gg 1$ and $\mathcal{D} \ll 1$ or $\mathcal{K} \ll 1$, which is possible in our experiments if the surfactant contaminants are strong and in relatively low concentrations. This is possible if contaminants are only hydrophobic PDMS chains. We solve the one-dimensional time-dependent advection equation for the transport of surfactants at the interface. Eq. S17 simplifies to, in nondimensional form,

$$\frac{\partial \hat{\Gamma}}{\partial \hat{t}} + \frac{\partial (\hat{u}_I \hat{\Gamma})}{\partial \hat{x}} = 0. \quad [\text{S32}]$$

In addition, because $Re = UH/\nu \ll 1$, viscous spreading across the channel height occurs very quickly compared with surfactant advection, and we approximate $(\partial \hat{u} / \partial \hat{z})_I$ as \hat{u}_I / \hat{H} in the left-hand side of [S29]. Given that the surfactant concentration is very small, $\hat{\Gamma} \ll 1$, the right-hand side of [S29] can be linearized to give

$$\frac{\hat{u}_I}{\hat{H}} = -Ma \frac{\partial \hat{\Gamma}}{\partial \hat{x}}. \quad [\text{S33}]$$

Substituting \hat{u}_I from [S33] into [S32], we find the conservation equation for $\hat{\Gamma}$:

$$\frac{\partial \hat{\Gamma}}{\partial \hat{t}} - Ma\hat{H} \frac{\partial}{\partial \hat{x}} \left(\hat{\Gamma} \frac{\partial \hat{\Gamma}}{\partial \hat{x}} \right) = 0. \quad [\text{S34}]$$

We introduce the similarity variables

$$\eta = \frac{1 + \hat{\ell}/2 - \hat{x}}{(\hat{t}Ma\hat{H})^{1/3}}, \quad [\text{S35}]$$

$$\hat{\Gamma}(x, t) = (\hat{t}Ma\hat{H})^{-1/3} f(\eta). \quad [\text{S36}]$$

Substituting into [S34], integrating twice, and using the boundary condition S30, the solution is

$$\hat{\Gamma}(x, t) = \frac{C}{(\hat{t}Ma\hat{H})^{1/3}} - \frac{(1 + \hat{\ell}/2 - \hat{x})^2}{6\hat{t}Ma\hat{H}}, \quad [\text{S37}]$$

which is valid for \hat{t} larger than diffusion time (i.e., at very small \hat{t} diffusion plays a role) and for time small enough that the front of the advection $\hat{x}_f(\hat{t})$ is still between the two stagnation points, $\hat{\ell}/2 \leq \hat{x}_f \leq 1 + \hat{\ell}/2$. For the initial condition, if we assume that the loading phase had a strong positive background flow (such as in the pressure-relaxation experiments), then surfactants have accumulated near the downstream stagnation point $\hat{x} = 1 + \hat{\ell}/2$ for $\hat{t} \leq 0$. The exact distribution of the surfactants at $\hat{t} = 0$ is unknown, but in the stagnant cap regime, we can assume that it is steep near $\hat{x} = 1 + \hat{\ell}/2$. The constant of integration C is effectively a measure of the total amount of surfactant on the interface, which is constant at all times under our assumption of negligible exchanges with the bulk. This is effectively the main unknown in our experiments. We find

$$C = \left(\frac{\sqrt{3}}{2\sqrt{2}} \int_{\hat{x}_f}^{1+\hat{\ell}/2} \hat{\Gamma} d\hat{x} \right)^{2/3}, \quad [\text{S38}]$$

where $\hat{x}_f(\hat{t})$ is the front of the surfactant; i.e., where Γ vanishes,

$$\hat{x}_f = 1 + \hat{\ell}/2 - \sqrt{6C} (\hat{t}Ma\hat{H})^{1/3}, \quad [\text{S39}]$$

which is effectively valid in our finite-length geometry until the front reaches the stagnation point at $\hat{x} = \hat{\ell}/2$, as the model assumes a semi-infinite lane $\hat{x} \leq 1 + \hat{\ell}/2$. From [S33] and [S37], the interfacial speed due to surfactant gradients is therefore

$$\hat{u}_I = -\frac{1 + \hat{\ell}/2 - \hat{x}}{3\hat{t}}. \quad [\text{S40}]$$

Thus, \hat{u}_I is negative, corresponding to the backflow observed in our experiments (Fig. 4 A and B) for $\hat{t} > 0$. Once the loading phase ends and the background flow stops, the surfactants travel back along the interface, driving a Marangoni backflow, to eventually redistribute uniformly along the air–water interface, $\hat{\ell}/2 \leq \hat{x} \leq 1 + \hat{\ell}/2$. This result also shows that the backflow velocity should decrease in time as $1/\hat{t}$. We compare this scaling prediction with our experimental results in Fig. 4D. As mentioned previously, this result is not valid at very small time, where diffusion processes and the unknown initial distribution of the surfactant have a strong influence on the Marangoni-driven flow. Hence, it cannot inform us about the dependence of the peak backflow velocity, measured at $\hat{t} \approx 0$, with U (Fig. 4C). It informs us only about the trend of the backflow at intermediate times, as shown in Fig. 4D, until the opposite stagnation point at $\hat{x} = \hat{\ell}/2$ starts playing a role. We also note that the interfacial velocity estimated in [S40] does not depend on the Marangoni number or on any other parameters. It depends only on the local gradient of the interfacial surfactant distribution, which depends on time and the spatial coordinate.

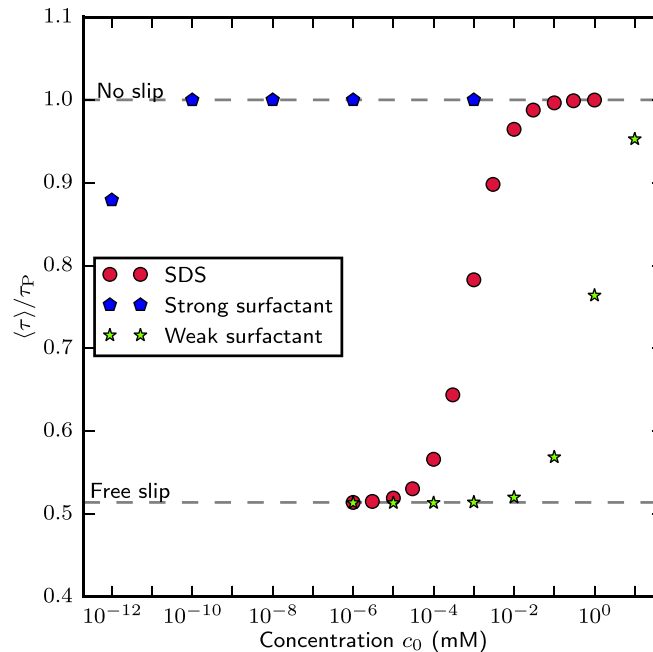


Fig. S1. Simulations of surfactant-laden flows in the 2D model SHS chamber shown in Fig. 2A. We compare the averaged normalized drag vs. the surfactant concentration for varying surfactant properties, using Frumkin kinetics. The SDS properties and the properties of the weak and strong model surfactants (defined using the extreme property values reported in ref. 40) are presented in Table S1. The associated characteristic nondimensional numbers of the SDS and the strong and weak model surfactants are presented in Table S2. The behavior of the transition is similar for all three surfactants, but it occurs at different concentration thresholds. The threshold is particularly low for the strong surfactant, $c_0 \leq 10^{-10}$ mM.

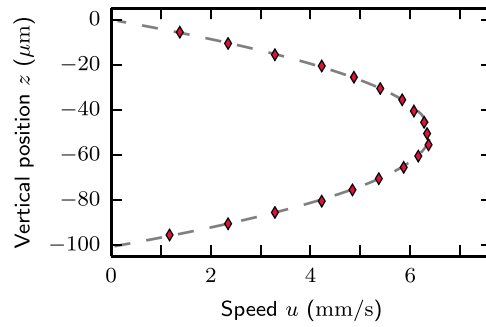


Fig. S2. Vertical distribution of the stream-wise velocity profile during the loading phase of the experiment presented in Fig. 4A. The dashed line shows the result of a parabolic fit of the velocity profile. The mean speed of the flow extracted from this fit is $U \approx 3.9 \text{ mm}\cdot\text{s}^{-1}$.

Table S1. Parameters for 2D surfactant-laden simulations (Fig. 2 and Fig. S1)

Parameter	Symbol	Value	Unit	Use
Grating length	g	1×10^2 $20\text{--}10^4$	μm μm	Fig. 2 B–D and Fig. S1 Fig. 2E
Bulk concentration	c_0	1×10^{-6} 1×10^{-2} $10^{-6}\text{--}1$ $10^{-12}\text{--}10^{-3}$ $10^{-6}\text{--}10$	$\text{mol}\cdot\text{m}^{-3}$ $\text{mol}\cdot\text{m}^{-3}$ $\text{mol}\cdot\text{m}^{-3}$ $\text{mol}\cdot\text{m}^{-3}$ $\text{mol}\cdot\text{m}^{-3}$	Fig. 2B Fig. 2 C and E Fig. 2D Fig. S1, strong surfactant (blue symbols) Fig. S1, weak surfactant (green symbols)
Chamber height	H	1×10^2	μm	
Ridge length	ℓ	5×10^1	μm	
Maximum forcing speed	u_{max}	5×10^1	$\mu\text{m}\cdot\text{s}^{-1}$	
Mean forcing speed	U	3.3×10^1	$\mu\text{m}\cdot\text{s}^{-1}$	
Water viscosity	μ	8.9×10^{-4}	$\text{N}\cdot\text{s}\cdot\text{m}^{-2}$	
Water surface tension	σ_0	72×10^{-3}	$\text{N}\cdot\text{m}^{-1}$	
Bulk diffusivity	D	7×10^{-10} 1×10^{-11} 1×10^{-9}	$\text{m}^2\cdot\text{s}^{-1}$ $\text{m}^2\cdot\text{s}^{-1}$ $\text{m}^2\cdot\text{s}^{-1}$	Fig. 2 B–E Fig. S1, strong surfactant (blue symbols) Fig. S1, weak surfactant (green symbols)
Surface diffusivity	D_s	7×10^{-10} 1×10^{-11} 1×10^{-9}	$\text{m}^2\cdot\text{s}^{-1}$ $\text{m}^2\cdot\text{s}^{-1}$ $\text{m}^2\cdot\text{s}^{-1}$	Fig. 2 B–E Fig. S1, strong surfactant (blue symbols) Fig. S1, weak surfactant (green symbols)
Desorption coefficient	κ_d	500 1 100	s^{-1} s^{-1} s^{-1}	Fig. 2 B–E Fig. S1, strong surfactant (blue symbols) Fig. S1, weak surfactant (green symbols)
Adsorption coefficient	κ_a	89.5 1×10^6 1×10^{-1}	$\text{m}^3\cdot\text{mol}^{-1}\cdot\text{s}^{-1}$ $\text{m}^3\cdot\text{mol}^{-1}\cdot\text{s}^{-1}$ $\text{m}^3\cdot\text{mol}^{-1}\cdot\text{s}^{-1}$	Fig. 2 B–E Fig. S1, strong surfactant (blue symbols) Fig. S1, weak surfactant (green symbols)
Maximum packing concentration	Γ_m	3.9×10^{-6} 1×10^{-5} 1×10^{-6}	$\text{mol}\cdot\text{m}^{-2}$ $\text{mol}\cdot\text{m}^{-2}$ $\text{mol}\cdot\text{m}^{-2}$	Fig. 2 B–E Fig. S1, strong surfactant (blue symbols) Fig. S1, weak surfactant (green symbols)
Interaction coefficient	A	–2.4 –3 3	— — —	Fig. 2 B–E Fig. S1, strong surfactant (blue symbols) Fig. S1, weak surfactant (green symbols)
Surfactant style constant	n	2	—	

Table S2. Nondimensional parameters associated with Table S1 for 2D surfactant-laden simulations (Fig. 2 and Fig. S1)

Parameter	Fig. 2B	Fig. 2C	Fig. 2D	Fig. 2E	Fig. S1, strong surfactant	Fig. S1, weak surfactant
$Re = HU/\nu$	3.7×10^{-3}	3.7×10^{-3}	3.7×10^{-3}	3.7×10^{-3}	3.7×10^{-3}	3.7×10^{-3}
$Pe = gU/D$	4.7	4.7	4.7	0.9–470	330	3.3
$Pe_s = gU/D_s$	4.7	4.7	4.7	0.9–470	330	3.3
$k = \kappa_a c_0 / \kappa_d$	1.8×10^{-7}	1.8×10^{-3}	1.8×10^{-7} –0.18	1.8×10^{-3}	10^{-6} – 10^3	10^{-9} – 10^{-2}
$Bi = g\kappa_d/U$	1.5×10^3	1.5×10^3	1.5×10^3	300– 1.5×10^5	3	300
$\chi = g\kappa_d/(\kappa_a \Gamma_m)$	140	140	140	30– 1.4×10^4	10^{-5}	10^5
$Ma = nRT\Gamma_m/(\mu U)$	6.6×10^5	6.6×10^5	6.6×10^5	6.6×10^5	1.7×10^6	1.7×10^5
$\hat{H} = H/g$	1	1	1	5–0.01	1	1
$\hat{\ell} = \ell/g$	0.5	0.5	0.5	2.5 – 5×10^{-3}	0.5	0.5
$\mathcal{D} = \chi(1+k)/Pe^{1/2}$	66	66	66–77	30–660	6×10^{-7} – 5×10^{-4}	5.5×10^4 – 5.6×10^4
$\mathcal{K} = Bi(1+k)$	1.5×10^3	1.5×10^3	1.5×10^3 – 1.8×10^3	300– 1.5×10^5	3 – 3×10^3	300 [†]

[†]The variation of this parameter across the range of concentrations is not significant.

Table S3. Parameters for steady-forcing experiments (Fig. 3)

Parameter	Symbol	Value		Unit
		Fig. 3D	Fig. 3E	
Grating length	g	2	30	mm
Grating width	w	4×10^1	4×10^1	μm
Chamber height	H	1.3×10^2	1.0×10^2	μm
Ridge length	ℓ	2×10^1	2×10^1	μm
Ridge width	r	2×10^1	2×10^1	μm
Max. forcing speed	u_{max}	1.1×10^2	1.3×10^2	$\mu\text{m}\cdot\text{s}^{-1}$
Mean forcing speed	U	7.3×10^1	8.7×10^1	$\mu\text{m}\cdot\text{s}^{-1}$
Temperature	T	23	23	$^\circ\text{C}$

Table S4. Nondimensional parameters associated with Table 4 for steady-forcing experiments (Fig. 3)

Parameter	Fig. 3D, assuming weak surfactant	Fig. 3D, assuming strong surfactant	Fig. 3E, assuming weak surfactant	Fig. 3E, assuming strong surfactant
$Re = HU/\nu$	0.01	0.01	9×10^{-3}	9×10^{-3}
$Pe = gU/D$	150	1.5×10^4	2.6×10^3	2.6×10^5
$Pe_s = gU/D_s$	150	1.5×10^4	2.6×10^3	2.6×10^5
$k = \kappa_a c_0 / \kappa_d$	10^{-15} – 10^{-3}	10^{-6} – 10^6	10^{-15} – 10^{-3}	10^{-6} – 10^6
$Bi = g\kappa_d/U$	2.7×10^3	27	3.4×10^4	340
$\chi = g\kappa_d/(\kappa_a \Gamma_m)$	2×10^6	2×10^{-4}	3×10^7	3×10^{-3}
$Ma = nRT\Gamma_m/(\mu U)$	7.3×10^4	7.3×10^5	6.1×10^4	6.1×10^5
$\hat{H} = H/g$	6.5×10^{-2}	6.5×10^{-2}	3.3×10^{-3}	3.3×10^{-3}
$\hat{\ell} = \ell/g$	2.5×10^{-2}	2.5×10^{-2}	1.7×10^{-3}	1.7×10^{-3}
$\mathcal{D} = \chi(1+k)/Pe^{1/2}$	$1.7 \times 10^{5\dagger}$	1.7×10^{-6} –1.7	$5.9 \times 10^{5\dagger}$	5.9×10^{-6} –5.9
$\mathcal{K} = Bi(1+k)$	$2.7 \times 10^{3\dagger}$	27 – 2.7×10^7	3.4×10^4 – 3.5×10^4	340 – 3.4×10^8

Note that we assume the kinetics properties of the weak and strong surfactants described in Table 1, with a range of concentrations from $c_0 = 10^{-12}$ to $1 \text{ mol}\cdot\text{m}^{-3}$.

[†]The variation of this parameter across the range of concentrations is not significant.

Table S5. Parameters for 3D surfactant-free simulations (Fig. 3)

Parameter	Symbol	Value	Unit	Use
Bulk concentration	c_0	0	$\text{mol}\cdot\text{m}^{-3}$	
Grating length	g	2	mm	Fig. 3D
		30	mm	Fig. 3E
Grating width	w	4×10^1	μm	
Chamber height	H	1.3×10^2	μm	Fig. 3D
		1.0×10^2	μm	Fig. 3E
Ridge length	ℓ	2×10^1	μm	
Ridge width	r	2×10^1	μm	
Maximum forcing speed	u_{max}	1.2×10^2	$\mu\text{m}\cdot\text{s}^{-1}$	
Mean forcing speed	U	8×10^1	$\mu\text{m}\cdot\text{s}^{-1}$	
Water viscosity	μ	9.3×10^{-4}	$\text{N}\cdot\text{s}\cdot\text{m}^{-2}$	

Table S6. Experimental parameters of all of the pressure-relaxation experiments

Experiment	ΔH_r , mm	U , mm/s	Note
1-1	70	4.4	
1-2	-70	3.9	
1-3	70	4.3	
1-4	-70	3.9	
1-5	70	4.3	
1-6	-70	3.8	
1-7	70	4.3	
1-8	-70	3.8	
2-1	100	5.4	Adjacent grating failed
2-2	100	4.8	Adjacent grating failed
2-3	100	5.3	Adjacent grating failed
2-4	100	4.4	Adjacent grating failed
3-1	-40	2.3	
3-2	40	2.5	
3-3	-40	2.3	
3-4	40	2.5	
3-5	-40	2.3	
3-6	40	2.5	
3-7	-40	2.3	
3-8	40	2.4	Adjacent grating failed
3-9	-40	2.2	Adjacent grating failed
3-10	40	2.4	Adjacent grating failed
3-11	-40	2.2	Grating under study failed
3-12	40	2.5	Adjacent grating failed
4-1	130	7.4	Adjacent grating failed

Table S7. Nondimensional parameters for pressure-relaxation experiments in the loading phase (Fig. 4)

Parameter	$U = 2.3 \text{ mm} \cdot \text{s}^{-1}$, assuming weak surfactant	$U = 2.3 \text{ mm} \cdot \text{s}^{-1}$, assuming strong surfactant	$U = 4.1 \text{ mm} \cdot \text{s}^{-1}$, assuming weak surfactant	$U = 4.1 \text{ mm} \cdot \text{s}^{-1}$, assuming strong surfactant
$Re = HU/\nu$	0.25	0.25	0.44	0.44
$Pe = gU/D$	6.9×10^4	6.9×10^6	1.2×10^5	1.2×10^7
$Pe_s = gU/D_s$	6.9×10^4	6.9×10^6	1.2×10^5	1.2×10^7
$k = \kappa_a c_0 / \kappa_d$	$10^{-15} - 10^{-3}$	$10^{-6} - 10^6$	$10^{-15} - 10^{-3}$	$10^{-6} - 10^6$
$Bi = g\kappa_d/U$	1.3×10^3	13	730	7
$\chi = g\kappa_d / (\kappa_a \Gamma_m)$	3×10^7	3×10^{-3}	3×10^7	3×10^{-3}
$Ma = nRT\Gamma_m / (\mu U)$	2.3×10^3	2.3×10^4	1.3×10^3	1.3×10^4
$\hat{H} = H/g$	3.3×10^{-3}	3.3×10^{-3}	3.3×10^{-3}	3.3×10^{-3}
$\hat{\ell} = \ell/g$	1.7×10^{-3}	1.7×10^{-3}	1.7×10^{-3}	1.7×10^{-3}
$\mathcal{D} = \chi(1+k)/Pe^{1/2}$	$1.1 \times 10^{5\dagger}$	$1.1 \times 10^{-6} - 1.1$	$8.6 \times 10^4\dagger$	$8.6 \times 10^{-7} - 0.9$
$\mathcal{K} = Bi(1+k)$	$1.3 \times 10^3\dagger$	$13 - 1.3 \times 10^7$	730 [†]	$7.3 - 7.3 \times 10^6$

Note that we assume the kinetic properties of the weak and strong surfactants described in Table S1, with a range of concentrations from $c_0 = 10^{-12}$ to $1 \text{ mol} \cdot \text{m}^{-3}$.

[†]The variation of this parameter across the range of concentrations is not significant.

